Design and Evaluation of Multispectral LiDAR for the Recovery of Arboreal Parameters

Andrew M. Wallace, Aongus McCarthy, Caroline J. Nichol, Ximing Ren, Simone Morak, Daniel Martinez-Ramirez, Iain H. Woodhouse, and Gerald S. Buller

***Abstract*—Multispectral light detection and ranging (LiDAR) has the potential to recover structural and physiological data from arboreal samples and, by extension, from forest canopies when deployed on aerial or space platforms. In this paper, we describe the design and evaluation of a prototype multispectral LiDAR system and demonstrate the measurement of leaf and bark area and abundance profiles using a series of experiments on tree samples "viewed from above" by tilting living conifers such that the apex is directed on the viewing axis. As the complete recovery of all structural and physiological parameters is ill posed with a restricted set of four wavelengths, we used leaf and bark spectra measured in the laboratory to constrain parameter inversion by an extended reversible jump Markov chain Monte Carlo algorithm. However, we also show in a separate experiment how the multispectral LiDAR can recover directly a profile of Normalized Difference Vegetation Index (NDVI), which is verified against the laboratory spectral measurements. Our work shows the potential of multispectral LiDAR to recover both structural and physiological data and also highlights the fine spatial resolution that can be achieved with time-correlated single-photon counting.**

***Index Terms*—Leaf area profile, leaf physiology, light detection and ranging (LiDAR), multispectral, parameter inversion.**

I. Introduction

AERIAL or space-based measurements using a multispectral canopy light detection and ranging (LiDAR) (MSCL) could provide improved estimates of carbon sequestration and existing forest stocks, allowing us to better understand climate change and the seasonal dynamics of ecosystem carbon uptake in response to environmental drivers such as water, temperature, light, and nutrient availability. Ultimately, we seek to detect seasonal changes in photosynthesis, photosynthetic light use efficiency [1], and stress within forest canopies using MSCL as part of a larger sensor suite on air [2] or space [3] borne platforms. MSCL can provide information on the vertical distribution of optical properties which can then be used to infer physiological processes directly linked to actual carbon sequestration as well as carbon stocks and can disambiguate ground from canopy returns.

Passive hyperspectral sensors rely on reflected solar radiation, and spectral ratios or indices can be measured that can be precisely related to physiological properties, such as leaf chlorophyll content, water content, and stress [4]–[6]. Provided that leaf abundance is known or measured, pigments within the leaves, including chlorophyll a and b, can be used as effective indicators of the physiological health of the forest canopy [7]. However, passive sensors give an integrated measurement in the direction of view, report data in two dimensions only, and therefore cannot fully resolve, for example, the 3-D structure of an old growth forest and, therefore, all photosynthesizing elements, which is critical if a whole canopy calculation of forest carbon flux is to be achieved. The chlorophyll content within leaves is dependent on species type, needle age, and the illumination conditions and is expected to vary with the depth within the canopy, which cannot be resolved by the integrated hyperspectral image. Consequently, algorithms for parameter recovery effectively combine spectral unmixing [8], [9] with the variation of the spectra themselves, as these give the parameters of interest, and hence, such algorithms may be ill posed. Although it is also possible to estimate structural parameters such as leaf area index (LAI) and canopy above ground biomass [4] from passive data, these estimates rely on *a priori* assumptions from previously collected data on known tree stock distribution and allometric relationships [10]. Hill [5] discusses how forest architecture (species, senescent leaves, soil, and understory vegetation) and angle effects (sensor and source/sun) significantly impact such existing empirical relationships, which include implicitly or explicitly models to quantity the distribution and orientation of foliage, including Weibull [11] and beta functions [12]. However, reliance on *a priori* knowledge of species and location does not replicate direct LiDAR measurements.

Laser altimetry or LiDAR is a well-established tool used both in terrestrial and airborne platforms to provide detailed measurements of vegetation structure, increasingly required to support a range of research themes from sustainable forest management to carbon accounting [13]. In particular, it is possible to recover structural parameters from terrestrial, air, and space borne LiDAR systems [14], [15]. Mallet and Bretar [16]

Manuscript received December 4, 2012; revised July 10, 2013; accepted September 9, 2013. Date of publication November 21, 2013; date of current version March 3, 2014. This work was supported in part by the Engineering and Physical Sciences Research Council under Grant references EP/H022414/1, "Developing full waveform, Bayesian analysis for multispectral canopy LiDAR images," and EP/J015180, "Sensor Signal Processing," and in part by the Centre for Earth Observation and Instrumentation under Contract Number 4500134278, "Demonstrating the quantitative recovery of structural and biochemical parameters from forest canopies using a new hyper-spectral LiDAR." The work of D. Martinez-Ramirez was supported by Conacyt.

A. M. Wallace, A. McCarthy, X. Ren, D. Martinez-Ramirez, and G. S. Buller are with the School of Engineering and Physical Sciences, Heriot-Watt University, Edinburgh EH14 4AS, U.K. (e-mail: a.m.wallace@hw.ac.uk; a.mccarthy@hw.ac.uk; xr5@hw.ac.uk; dsm21@hw.ac.uk; g.s.buller@hw.ac.uk).

C. J. Nichol, S. Morak, and I. H. Woodhouse are with the School of Geosciences, Edinburgh University King's Buildings, Edinburgh EH9 3JN, U.K. (e-mail: caroline.nichol@ed.ac.uk; s.morak@reading.ac.uk; i.h.woodhouse@ed.ac.uk).

Color versions of one or more of the figures in this paper are available online at http://ieeexplore.ieee.org.

Digital Object Identifier 10.1109/TGRS.2013.2285942

and Leuwen and Nieuwenhuis [17] give excellent reviews of remote sensing by LiDAR, and we refer the interested reader to these papers for a full description of the state of the art. They describe the recovery of key parameters, including tree or canopy height, LAI, fractional cover, foliage height profile, biomass and tree volume, terrain, and terrain slope and, by extension, species classification. In most systems, the parameter recovery is based on simple assumptions, for example, tree height can be measured by the separation of a "first" return from a "ground" return. However, the spatial distribution of leaf area within a canopy is a primary element of crown architecture as it exerts strong influence of the availability of light within the crown, thereby affecting the growth and performance of tree stands. Quantifying the vertical and the horizontal distribution of foliage can provide insight on the conversion of light into above ground biomass within the canopy and provide verifiable data for growth and climate modeling.

Full waveform analysis can give a much better idea of the intermediate vertical canopy structure. Monochromatic LiDAR data are complementary to hyperspectral imagery and cannot measure spectral indices directly. The obvious improvement is to obtain structural and physiological estimates by combining passive hyperspectral data with LiDAR data [18], [19]. For example, Swanatron *et al.* [20] report that combining active LiDAR data from the Laser Vegetation Imaging Sensor with passive hyperspectral data from the Airborne Visible Infrared Imaging Spectrometer can improve estimates of biomass and can better discriminate vegetation types in different forest environments. This combination is, however, often challenging to interpret because it is very difficult to accurately synchronize the data in time and space, and the integrated spectral data are not a full intensity profile along a multiple ray path that defines the pixel area or footprint. Hence, there is a priority to develop an MSCL capability that can determine not only structure but also physiological variation along the depth profile generated by a full waveform system.

Interest in multiple wavelength LiDAR technology is proceeding apace. The active airborne photon counting LiDAR, Slope Imaging Multi-polarization Photon Counting LiDAR [21], is a dual channel system operating at 532 and 1064 nm that measures within parallel and perpendicular polarization channels. Following an earlier study with a virtual MSCL that combined a monochromatic LiDAR with passive hyperspectral imaging [22], Hakala *et al.* [23] have built a system using a supercontinuum laser source and eight wavelength detectors to conduct laboratory measurements on Sitka spruce, deriving simple vegetation indices. Wei *et al.* [24] have also developed a full four-wavelength system, applying it to a segmentation problem using nine material classes. We have used the photon-counting approach to demonstrate excellent resolution of closely spaced surfaces in a previous multispectral system [25] and have shown using simulated and real experimental data how simple indices such as the Normalized Difference Vegetation Index (NDVI) [26] and Photochemical Reflectance Index (PRI) [27] can be measured along a laser profile [28].

In this paper, we report a new MSCL design using a supercontinuum laser source. We conduct field trials and manual validation on a single tree specimen to mimic an aerial measurement and develop our previous analyses of full waveforms [29] to interpret those data. In comparison with other groups, we harness the advantages of improved depth resolution and sensitivity that the time-correlated single-photon counting (TCSPC) technique brings to a supercontinuum source. We have also combined sensitive instrumentation with a direct parameter recovery process based on Markov chain Monte Carlo analysis that has greater potential to resolve the ambiguous interpretation of the field data. An earlier study [30] was able to resolve structure and chlorophyll content on multispectral data simulated from a real monospectral response. Here, we go further in interpreting full real multispectral data from tree samples and extending our analysis to include the estimation of plant area indices and abundance profiles, comparing spectral indices with controlled laboratory measurements.

The study reported here is at a small scale with small footprint LiDAR sampling a single tree and is thus intermediate between the leaf and canopy scale. However, it demonstrates a real multispectral LiDAR instrument that is the descendant of the previous instrument used at kilometer range [25], and we have calculated that this can be scaled up for aerial [2] and space [3] deployment. The extensive simulations of MSCL transport in simulated forest canopies [31], [32] also point to the feasibility of such an instrument. As our measurements are at short range (approximately 45 m), we do not consider the effects of atmospheric transmission, but we calibrate the system over the same range using standard targets. Spatially sampled MSCL extracts structure and physiology directly in three dimensions, and the source-sensor geometry is on the line of sight, so we use simplified optical models. Of course, that does not imply that multiple reflections and material angular distributions have no impact on measurement but that the coincident sensor geometry makes the problem more tractable.

This paper is organized as follows. In Section II, we describe the instrument design and construction. In Section III, we describe the calibration and characterization of the instrument and the collection of data from live tree samples on our site. We describe the laboratory measurements of the reflectance spectra of needles and bark for one such sample in Section IV. This allows the direct comparison of depth variation of one common index, NDVI, between passively and actively acquired wavelength measurements in Section V. In Section V, we also describe and apply the parameter inversion process to recover leaf and needle area and abundance profiles. Finally, in Section VI, we discuss our results and infer the necessary further research toward full canopy measurement with MSCL.

II. Design and Construction of the Multispectral LiDAR

The system employed for the measurements reported in this paper was designed and built for operation at the four wavelengths used commonly to compute the NDVI (670 nm, 780 nm) and PRI (530 nm, 570 nm) as these are good measures of the proportion of photosynthetic efficiency and green biomass, respectively [26], [27]. The principal components of

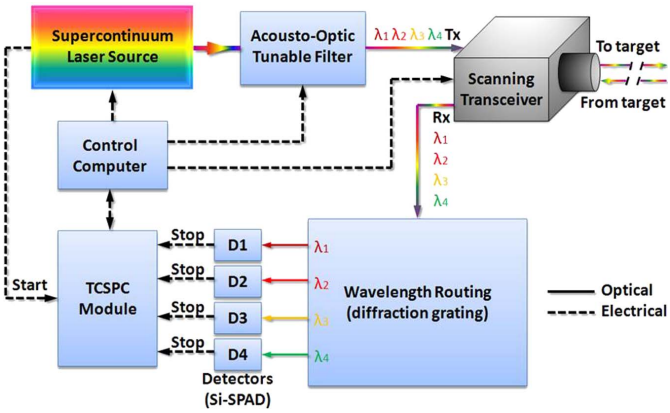

Fig. 1. Schematic diagram of the new multispectral time-of-flight TCSPC scanning system.

our four-wavelength system are shown schematically in Fig. 1, and the key parameters are summarized in Table I. The system was constructed mainly from modular components to allow flexibility in conducting experiments with a range of different source wavelengths and detectors.

The supercontinuum laser source (a SuperK EXTREME EXW-6, NKT Photonics, Denmark) emits over the 485–2400-nm wavelength range, and an integrated pulse picker module enables the selection of a preset pulse repetition rate of between approximately 320 kHz and 80 MHz. A tunable wavelength filter (a SuperK SELECT from NKT Photonics, Denmark) was used in conjunction with the supercontinuum source in order to isolate the appropriate wavelengths. This acousto-optic tunable filter (AOTF) configuration was capable of selecting up to eight different wavelengths between 500 and 850 nm. The spectral bandwidth of each of the four wavelengths used for this work was measured and found to be less than 8-nm full-width at half-maximum (FWHM), and the system emitted all wavelengths simultaneously.

The output of the AOTF was fiber coupled to the transmit channel of our custom-built scanning transceiver. This had previously been used for time-of-flight depth imaging field trials at a wavelength of 842 nm [33] and 1550 nm [34]. It was reconfigured with optical components appropriate for operation over the range of wavelengths used for the work reported in this paper. This custom unit is approximately 275 × 275 × 170 mm in size, excluding the objective lens which is interchangeable, allowing the use of lenses with different focal lengths and aperture diameters. The optomechanical system is based on a 25-mm-thick aluminum plate on which an appropriate network of fixed-width slots is accurately machined. Optical components such as the lenses, polarizing beam splitter, linear polarizer, and half-wave plate are mounted in 35-mm-diameter magnetic steel barrels. These barrels are positioned at the appropriate locations along the slots of the aluminum baseplate and held in position with magnets. This semikinematic approach is robust and provides flexibility, in terms of the layout of the optical system, as well as long-term mechanical stability. A pair of computer-controlled galvanometer mirrors, internal to the transceiver unit, enables all four coaxial illumination beams to be simultaneously scanned over the desired scene in two dimensions (x, y), allowing the collection of single footprint or 3-D depth image data. For each "pixel" of the scene, the scattered return photons that were collected by the system objective lens were steered by the galvanometer mirrors and coupled into a 9-μm-diameter core optical fiber connected to the receive channel of the transceiver. This fiber, used to link the receive channel to the wavelength routing module, had an armored tubing so as to minimize ambient light ingress into the fiber core along its length and at the connectors—this was a key factor that enabled measurements to be made under bright daylight conditions.

The wavelength routing module was similar in layout to the design of a previous multispectral LiDAR [25] system in that the spectral separation or demultiplexing of the four wavelengths in the armored fiber was achieved using a plane ruled reflection grating. The design of the optical system and associated optomechanics of this module allowed flexibility with the choice of wavelengths that could be accommodated and ease of reconfiguration. Therefore, a grating was used as opposed to an arrangement of spectral filters specific to each wavelength channel. The optomechanics of the wavelength routing module comprised a mix of custom and off-the-shelf components. The grating spatially separated the multiwavelength optical return, allowing each wavelength channel to be coupled to its individual detector (D1 to D4 as shown in Fig. 1) via a short length of optical fiber.

The configuration of the transceiver for operation at a single wavelength, as in previous depth imaging field trials [33], [34], included appropriate spectral filters in the receive channel in order to achieve the necessary filtering of the optical return signal. Ambient and solar background photons are a source of noise in a single-photon counting system as they cause "false" detection events at the detector. In previous configurations of this sensor, a narrow bandpass filter (matched to the laser wavelength) was typically used in conjunction with a short-pass and/or long-pass filter to minimize out-of-band radiation being incident on the detector. The filter combination was located immediately in front of the lens used to couple the return signal into the fiber connected to the detector. In this multiple-wavelength configuration, no spectral filters were used on the receive channel in the transceiver unit. The degree of spectral filtering achieved with the 1200 lines per millimeter plane ruled reflection grating, and the resulting spatial separation between the wavelength channels due to the layout of the module, meant that the out-of-band optical returns were sufficiently discriminated and not coupled to the detectors.

The four detectors were commercial thick-junction-Si Perkin–Elmer single-photon avalanche diode (SPAD) devices with high quantum efficiency and approximately 400-ps FWHM timing jitter. The system temporal response for each of the four individual wavelength channels is specified in Table I. The PicoQuant HydraHarp 400 data acquisition module collected data on four independent channels simultaneously with a maximum aggregate count rate of 12 megacounts per second, a 1-ps macrotime resolution, and a timing uncertainty less than 12 ps. The dead time is less than 80 ns. The full waveform timing data from the HydraHarp 400 are streamed to the computer by a universal serial bus (USB) connection.

TABLE I
SUMMARY OF KEY SYSTEM PARAMETERS

System Parameter	Comment
Transmit/Receive Alignment	Monostatic: the transmit and receive channels of all four wavelengths are coaxial.
Laser System	- NKT Photonics supercontinuum laser source (SuperK EXTREME EXW-6) - NKT Photonics acousto-optic tunable filter (SuperK SELECT) - Fiber-coupled to the transceiver unit
Laser Repetition Rate	2 MHz
Laser Pulse Width	< 50 ps
Illumination Wavelengths	531 nm, 570 nm, 670 nm, 780 nm (The pulses for all four wavelengths are emitted simultaneously)
Spectral Bandwidth	< 8 nm FWHM for each wavelength
Objective Lens	400 mm focal length, 142 mm diameter aperture (Canon FD 400 mm 1:2.8 L)
Average Output Power	< 200 µW total exiting the system
Range	Scans performed at a stand-off distance of 45 meters
Beam Scanning Mechanism	Galvanometer controlled mirrors (x & y) common to the transmit and receive channels
Collection Fiber	9 µm diameter core (SMF28), 2 meters long, armored
Spectral De-multiplexing	Plane ruled reflection grating, 1200 lines per mm
Detectors	Four similar Si-SPAD single-photon counting modules (Perkin Elmer), active area diameter 180 µm, thick junction, ~400 ps jitter, fiber-coupled, dark count rate < 500 c/s Quantum Efficiency (QE) as per manufacturer's data:

λ (nm)	531	570	670	780
QE (%)	~50	~58	~62	~58

System Temporal Response (jitter) – also see figure 3	**λ (nm)**	531	570	670	780
	FWHM (ps)	520	496	496	368

System Spatial Resolution (x-y)	~50 µrad
Data Acquisition Hardware	PicoQuant HydraHarp 400

III. MSCL CALIBRATION AND MEASUREMENT OF LIVE TREE SAMPLES

We calibrated the responses in each channel in time and amplitude and then proceeded to acquire meaningful data from tree samples. Previously, we conducted a series of measurements on tree samples at ranges of 45 and 325 m, using a single wavelength (842 or 1550 nm). We used these single-wavelength LiDAR data to simulate a multispectral response [29] using assumptions about material distribution and spectra. In this paper, we are able to report the first-daylight finely detailed (less than 1-cm resolution in x, y, and z) multispectral measurement and analysis of data from small tree samples at a standoff distance of 45 m. Furthermore, we have conducted laboratory measurements of the spectral response of the tree samples to validate the LiDAR measurement and parameter inversion.

A. Calibration Experiments

For these measurements, calibration targets and leaf and tree samples were mounted at a distance of 45 m from the LiDAR system, as shown in Fig. 2. We used a 400-mm-focal-length f/2.8 Canon objective lens which resulted in a beam spot diameter of approximately 3 mm on the targets and

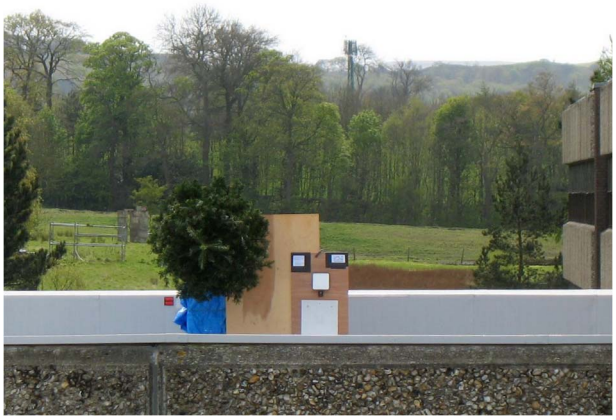

Fig. 2. Photograph showing a small conifer sample used for the experiments described here and several calibration targets, including the Spectralon panel.

samples. The pulse repetition rate was 2 MHz, and the total average optical output power exiting the transceiver across all four wavelengths (531, 570, 670, and 780 nm) was less than 200 μW. Four histograms, one for each wavelength, were acquired simultaneously for each pixel over 20 s using a binning size of 16 ps.

To ensure that the system gave stable operation, we conducted LiDAR measurement of reflection from the calibration target (i.e., a Spectralon panel from Labsphere) on all four channels before and after each tree measurement. The panel has a constant reflectance of greater than 99% between 531 and 780 nm. To ensure consistency of alignment, the panel was mounted on a tripod and placed directly in front of the tree apex for these measurements.

Fig. 3 shows an example of the system response, stable under repeated measurement. In this and in subsequent figures, the distance is measured from the sensor, and the zero position is offset from the sensor origin by the standoff distance, approximately 45 m. First, there are temporal offsets, caused by unequal electrical and optical fiber lengths in the system. These are easily compensated by shifting the received tree and leaf spectra into alignment. Second, the amplitudes are different, so we normalize channel amplitudes for tree data using these known Spectralon amplitudes. Third, the pulse shapes are similar but of slightly different widths. This means that we can use a distinct instrumental shape to process each channel separately.

B. Collection of Data From Live Tree Samples

We collected data from several live tree samples. The data presented here are from the sample and scanning pattern shown in Fig. 4.

Two full waveform LiDAR signals were recorded on the tree apex and on a patch of dense needle data, shown by the red crosses. A 10-by-10 image was scanned along the approximate grid shown from start to finish, i.e., by reversing the direction of the scan on each row. The pixel acquisition time was 20 s, i.e., the total scan time was approximately 34 min for 100 pixels. Fig. 5 shows a spectral response from the four channels for pixel 64 (fifth from the right on the seventh row

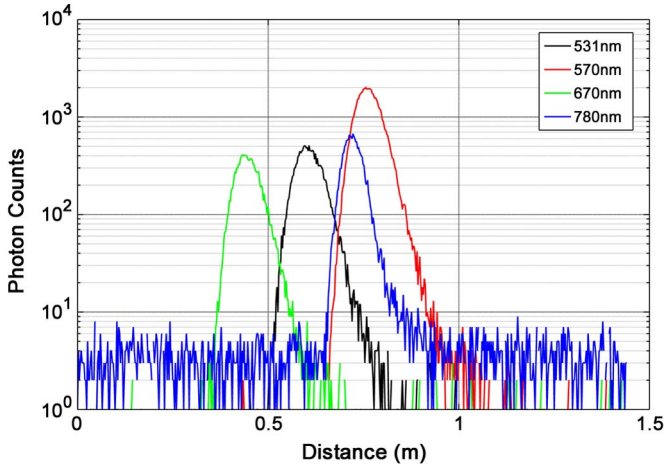

Fig. 3. Temporal response of LiDAR system (log scale) to Spectralon reflection for all four wavelengths. This gives calibration data for temporal shift, amplitude, and instrumental response of each channel. The FWHM of these responses is dominated by the timing jitter of the SPAD modules.

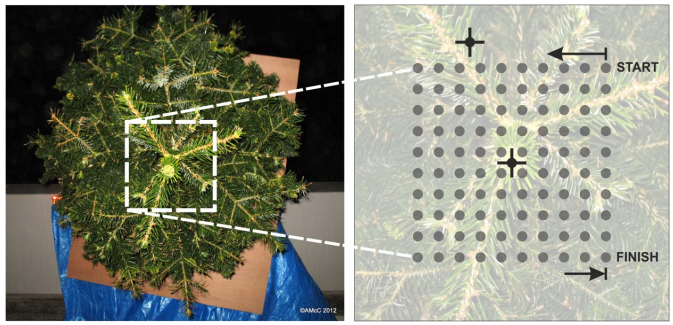

Fig. 4. Photograph of conifer sample and scan area and sampling grid along the LiDAR optical axis.

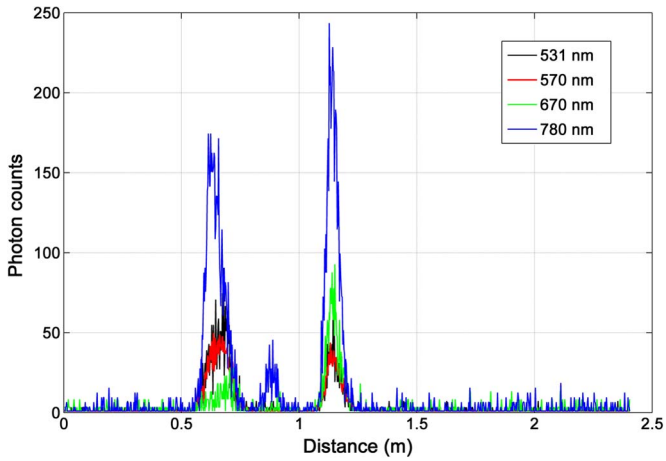

Fig. 5. Full waveform multispectral LiDAR data for a single pixel. This shows multiple responses through the canopy and differences in the spectral ratios.

down, as pixel count starts at zero). The horizontal axis is scaled to distance units (meters), but the origin is arbitrary just above the tree apex.

Fig. 6 shows the accumulated photon count responses for all 100 pixels, in which the bulk of the canopy returns is between approximately 0.6 and 1.5 m and the ground plane

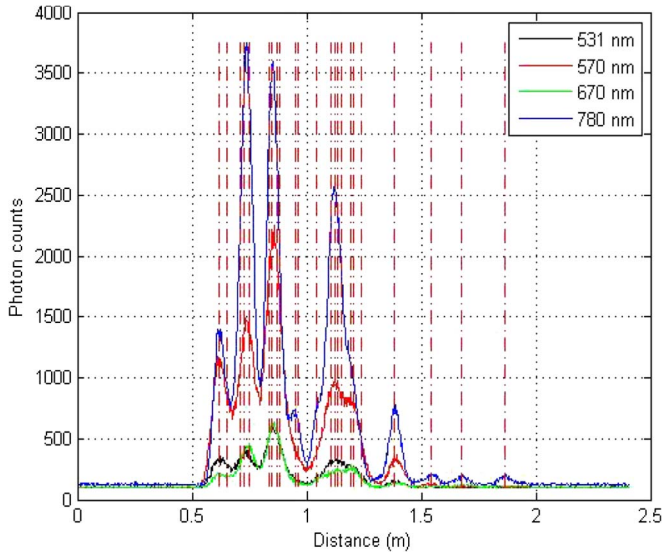

Fig. 6. Full waveform multispectral LiDAR data for ALL 100 pixels. The dotted lines show the recovered layer positions by the RJMCMC process (see Section V-A).

return is at approximately 1.8 m. The last return is of low amplitude because the tree crown is relatively dense. The dotted lines shown in Fig. 6 are the result of processing described in Section V. The tree height can be easily measured from such returns as approximately 1.2 m.

Examining Fig. 5, there are clear differences between the peak returns. The peaks at 0.7 and 1.2 m, for example, show a marked difference in the magnitude of the 670-nm channel with respect to the other channels. Only the 780-nm channel gives a significant response at the 0.9-m peak. The comparative reduction in amplitude of the 670-nm wavelength response at 0.7 m is consistent with a dip in the needle spectrum at that wavelength (see Section IV). However, the accumulated pixel response is, in general, a mixture of needle and bark response, and we must consider light penetration and absorption in the canopy. Therefore, there are inconsistencies between returns at a single pixel or returns from different pixels.

In contrast, the accumulated response in Fig. 6 shows more consistent behavior through the canopy. We might surmise that any misalignment in a receiver channel (as these are separate) might cause incorrect wavelength ratios for single pixels because the laser beam width is small, less than a needle length for example. Hence, the two channels may not be recording exactly the same material mixture. Nevertheless, accumulated sampling over many pixels and peaks compensates for outlying single point measurement and corresponds more closely to wider area measurement.

IV. Laboratory Measurement of Tree Spectra

Having collected MSCL field data, we removed the tree to the laboratory to conduct passive measurements of needle and bark spectral reflectance (with an Analytical Spectral Devices (ASD) FieldSpec PRO), as shown in Fig. 7. Our aim was to obtain true spectra that could be used to constrain the parameter inversion algorithms described in Section V and to allow a direct comparison of NDVI measured by the MSCL and the ASD.

Fig. 7. Passive measurement of the tree sample for validation. On the left are shown the stabilized light source and tripod-mounted spectrometer, with the several needle samples. On the right are shown the tree sample and the marked positions where the nine sets of needle samples were taken from the tree. Four bark samples were also taken.

Needle and bark samples were destructively sampled from the nine labeled heights through the profile of the tree and stacked densely in separate Petri dishes in random orientation. For each spectral measurement, the Petri dish was stacked on top of a further black Petri dish to be sure that the remaining light would be absorbed. As with the MSCL data, at the beginning between each sample, a spectral measurement was taken of the Spectralon panel. For each sample, we took four measurements, rotating the sample by 90° after each measurement to account for any orientation-dependent reflectance. This rotation allowed the clustered fibers within the bundle to view the entire sample within the dish. Without the rotations, each cluster of fibers represents a slightly different area.

The passive spectral measurements are plotted in Figs. 8 and 9. Within the region of interest, 531–980 nm, there are two key findings. First, the needle reflectance shows the expected "green peak" and "red edge," and the data are well, but not exactly, fitted by the Prospect model [35] which is used extensively to model leaf and needle optical properties, as shown in Fig. 10. This is consistent with the results by Malenovsky *et al.* [36] who observed only slight differences between the Prospect model and real Norway spruce needle data. To fit optimally the laboratory data, we extended the original set of four to eight wavelengths as that better allows us to define the "green peak" (531 nm, 550 nm, 570 nm) and the "red edge" (670 nm, 710 nm, 750 nm, 780 nm), with an additional wavelength at 970 nm which corresponds to a water absorption dip. This set of wavelengths retains the PRI and NDVI indices and is recommended for future work, although detection at 970 nm is challenging for silicon-based detectors. The bark or branch material also exhibits a significant red edge, as the samples were flecked with needle material. We present direct comparisons between the LiDAR and laboratory data and show how known spectra can be used in the recovery of abundance profiles in Section V.

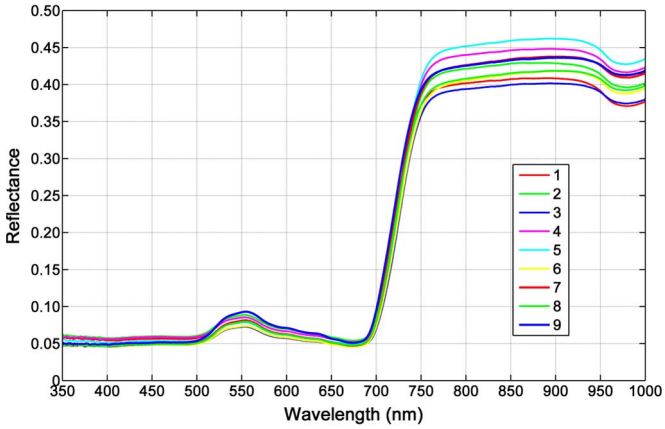

Fig. 8. Measured needle spectral reflectances from the nine samples, acquired by the apparatus shown in Fig. 7.

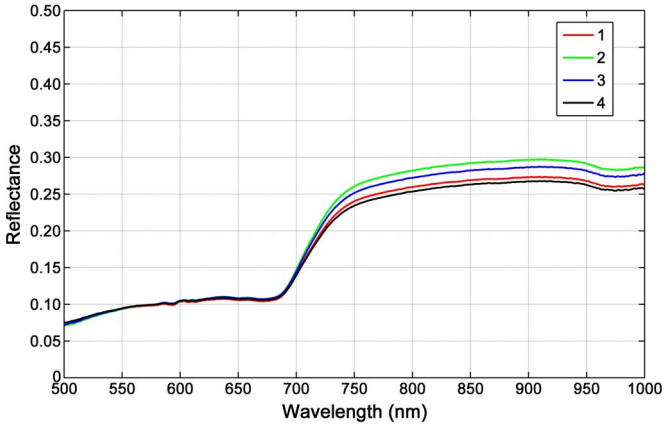

Fig. 9. Measured bark spectral reflectances from the four samples, acquired by the apparatus shown in Fig. 7.

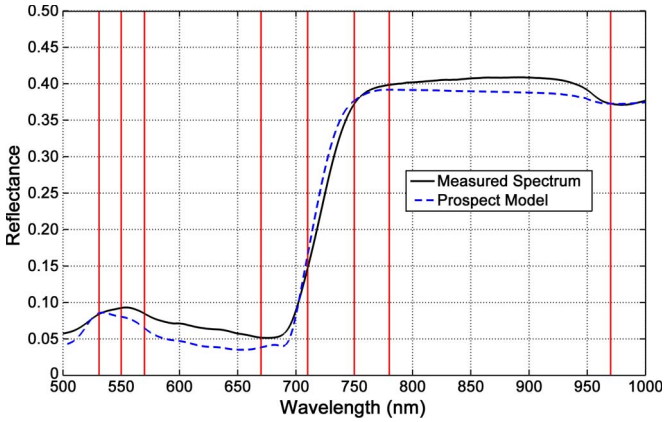

Fig. 10. Comparison of the (solid black line) true and (dashed blue line) best fitting Prospect spectra to the needle data. The rms fitting error is $2.36.10^{-2}$. It is not possible to fit the spectrum exactly by the Prospect model.

V. Parameter Inversion From an Arboreal Sample

The purpose of the proposed parameter inversion methodology is to combine the recovery of tree structure and material abundance with spectral variation that informs about tree physiology. However, four wavelengths are not sufficient to fully characterize the recovery of both abundance and needle physiology. The problem is ill posed. First, the Prospect model that we use to model the spectral response has at least six parameters; second, the relative abundance of woody elements affects the retrieval of physiological data [37]. Hence, we demonstrate that we are able to recover profiles that relate to tree structure and abundance, assuming known spectra. We further demonstrate that we can recover directly an NDVI profile using MSCL and compare this directly with laboratory ground truth.

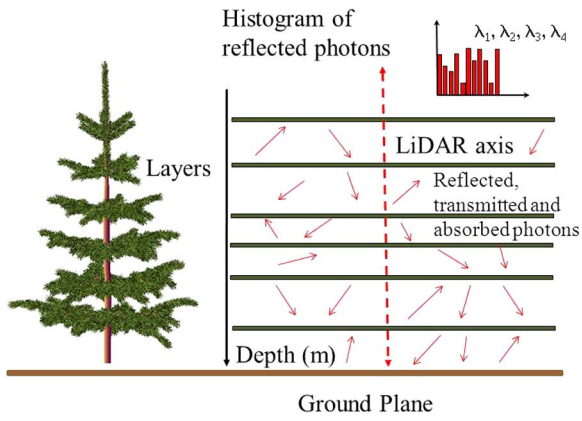

Fig. 11. Representation of forest or tree structure by a layered model. Unlike earlier models, e.g., [38], these layer positions are not fixed but recovered by a variable dimension analysis. This allows the parameter vector and synthesized response to adapt to the natural structure to give an excellent correspondence between the raw data and synthesized representation, as shown in Fig. 12.

A. RJMCMC Analysis to Recover Layer Positions and Signal Amplitudes

We now describe and evaluate the application of full waveform multispectral LiDAR analysis to the data of Fig. 6 to recover both the area distribution and the relative abundance of needle and bark material through the depth profile, using the reasonable *a priori* knowledge that there will not be significant variation in needle material in a single open sample, verified by laboratory measurements. The analysis here of multispectral data acquired from real tree samples in an outside environment highlights both what can be achieved and what is necessary to extend that analysis.

The process that we have adopted is to use the known spectral reflectance data from the samples to recover abundance and needle/bark area index profiles. We first apply the reversible jump Markov chain Monte Carlo (RJMCMC) analysis described in [29] to the 780-nm wavelength response. The explicit assumption is that we can represent the depth profile through the tree by a series of instrumental LiDAR returns from a set of "layers" at different depths, as shown in Fig. 11. In a tree or forest, there are countless surface responses from leaf, bark, and other surfaces, but we can represent the layered response by a series of virtual surfaces at depths recovered by RJMCMC analysis and then associate both structural and physiological parameters with each layer.

The value recorded in each bin of each wavelength in Fig. 6 is a random sample from a Poisson distribution that depends on

the sample parameters

$$p(y_{z,\lambda}|k,\omega,\varnothing) = \sum_{m,1}^{k}\sum_{l,1}^{R}\omega_{z,l}f(y_{z,\lambda}|k,\varnothing_{m,l}) + B_{\lambda} \quad (1)$$

where

- $y_{z,\lambda}$ is the photon count within a bin, indexed by z (distance) and λ (wavelength).
- k is the variable number of layers.
- R defines the number of materials (e.g., needles and bark) of the mixture.
- $\varphi_{m,l}$ is the parameter vector of the m th layer response for the l th component of the mixture. $\phi_l, [\phi_z, \phi_\lambda]$, where ϕ_z defines the temporal signature and ϕ_λ defines the spectral signature. The temporal signature is defined by the instrumental response, and the spectral signature is defined by the Prospect model.
- $f(.|.)$ describes the form of the photon impulse response function which is modeled by a piecewise exponential function explained fully in [29], whose shape parameters can differ between wavelength channels and is fitted from the Spectralon response. The normalized impulse response at depth z_0 is weighted by an amplitude factor β.
- $\omega_{z,l}$ defines the fraction or abundance of the l th component at distance z. These satisfy the conditions $\omega_{z,l} > 0$ for all z, l, and $\Sigma_{l,1}^{R}\omega_{z,l} = 1$.
- B_λ is a background and dark photon count level, constant in all bins at the same wavelength.
- $p(.|.)$ is a conditional probability distribution function.

The spectral response depends on both the relative abundance and the spectral signature of each mixture component. Assuming that the observations recorded in each channel are conditionally independent, given the values of the parameters, and each record is an independent measurement, the joint probability distribution of *y* is defined as

$$L(y|k,\omega,\phi) = \prod_{z,1}^{Z}\prod_{l,1}^{R} e^{-p(y_{z,\lambda}|k,\omega,\varnothing)}\frac{p(y_{z,\lambda}|k,\omega,\varnothing)^{y_{z,\lambda}}}{y_{z,\lambda!}}. \quad (2)$$

As it is not possible to have negative values of $y_{z,\lambda}$ and because the product tends to zero, we minimize -2ln $L(c/\phi)$ as is the common practice. To make inferences about the dimension k and the consequent parameter vector ϕ of our model given the data y, the likelihood L is combined with prior information P. This is summarized in a posterior or target distribution

$$\pi(k,\omega,\phi|y) = \frac{L(k,\omega,\phi|y)P(k,\omega,\phi)}{\int L(k,\omega,\phi|y)P(k,\omega,\phi)\delta(k,\omega,\phi)}. \quad (3)$$

With reference to Algorithm 1, Stage 1, at each iteration of the RJMCMC chain, there are two steps, a parameter-updating step with fixed dimension and a dimension-changing step that allows jumps between different numbers of returns. This latter increase or decrease can be achieved by a birth of a new return, a splitting of an existing return, a death of an existing return, or a merging of two existing returns.

Algorithm 1: The two-stage RJMCMC process to define the best fitting parameters, i.e., the peak positions and amplitudes and constant background level, that best represent a layered response using the best fitting Prospect model for needle reflectance and the measured bark reflectance.

Stage 1: Using a single wavelength: unknown number of layers, positions, and amplitudes

Fixed dimension (known number of layers, k):

- Update fixed parameter vector:
  - Update amplitude vector, β
  - Update position vector, z_o
- Update background value, B

Change of dimension, k:

- Birth/split of return/layer, increments k
- Death/merge of two returns/layers, decrement k

Stage 2: Using *all* wavelengths (fixed positions, known k)

- Update fixed parameter vector:
  - Update amplitude vector, β

Update background value, B

Using dimension-varying RJMCMC gives a much better representation of the data than a fixed equally spaced layer model [38] as the response is by no means uniform and is a convolution of the surface and instrumental responses. All four wavelengths have coincident beams, but the RJMCMC process involves random sampling of the posterior distribution. Therefore, if we process each wavelength response independently, we would expect to obtain different layer positions in each channel, even though the peak responses coincide generally as shown in Fig. 6. Therefore, we apply RJMCMC to the largest spectral return, invariably 780 nm, and then reapply an MCMC algorithm at Stage 2 to the other channels with fixed dimension and position vector, recovering only the return amplitudes.

This analysis resolves the positions and amplitudes as shown in Table II; the positions are the dotted lines illustrated in Fig. 6.

As the bin width is 16 ps, the peak separation of one bin corresponds to 2.4 mm (go–return). We have shown that TCSPSC technology can resolve effectively to 1.7 cm [29].

In these experiments, we do not have ground truth on surface positions (many of which may move in wind), and each layer response is an integration of many individual surface returns. However, Table II and Fig. 6 do show that the structural signature of the sample is approximated to a z-resolution on the order of centimeters, in contrast to systems based on much wider laser pulses [16]. The fits of the parameterized waveforms to the raw photon count data are excellent, as shown in Fig. 12, which shows a root mean square (rms) fitting error of 3.01 photons for the 780-nm data.

B. Determining the NDVI Profile in Comparison With the Laboratory Data

The data shown in Table II are not normalized; it has not been scaled by the known calibration response of the Spectralon data at each wavelength shown in Fig. 3. Furthermore, the calibration data have been taken for a single pixel, but the data

TABLE II
DIMENSION, POSITION, AND AMPLITUDE VECTORS FOR NORDMANN FIR

k	$t_{0\ (bins)}$	β_{531}	β_{570}	β_{670}	β_{780}
1	257	189.32	746.66	22.516	907.93
2	258	28.03	232.45	71.032	219.56
3	272	37.603	161.88	24.801	368.01
4	296	85.542	117.18	5.9293	565.35
5	304	71.066	559.47	197.83	1720.5
6	313	143.05	813.62	141.24	1866.9
7	348	24.487	253.09	8.7835	224.79
8	354	247.61	368.71	391.26	2649.6
9	362	202.71	1551.4	36.743	585.71
10	367	16.751	17.207	100.61	300.99
11	397	15.999	9.0193	6.9965	394.91
12	400	7.3048	108.79	2.7745	84.683
13	435	45.21	228.9	46.29	514.83
14	460	59.425	238.61	23.65	1206.5
15	467	144.88	545.70	106.48	550.00
16	474	10.287	76.12	6.2535	1015.5
17	479	15.271	70.755	12.497	319.54
18	496	99.264	224.85	19.091	120.58
19	501	28.429	321.35	122.91	593.27
20	515	27.587	94.926	2.8447	44.753
21	577	48.385	233.45	30.844	629.25
22	644	7.5651	29.048	5.1334	67.501
23	699	2.7824	10.535	19.372	51.357
24	778	4.7193	12.028	12.97	68.131
Background		99.63	99.54	102.64	120.78

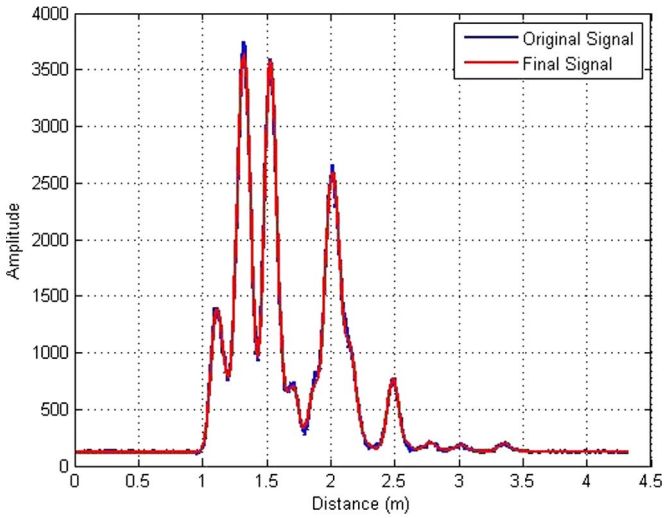

Fig. 12. Comparison of the raw data (780 nm, blue) against a waveform synthesized from the estimated parameters of Table I. The rms fitting error is 3.01 photons.

of Table II are summed over 100 pixels, so this must be taken into account. Doing this, one can determine the total relative reflectance of the tree sample against the Spectralon (assumed 100%) either by summing the fitted amplitudes or total photons returned.

The total reflectance levels are low but can be compared with data shown in [1] in which the measured absolute reflectance across the spectrum is shown to be much lower in coniferous than in deciduous forest canopies. Although we are operating at a much smaller scale, our measurement is on the central portion

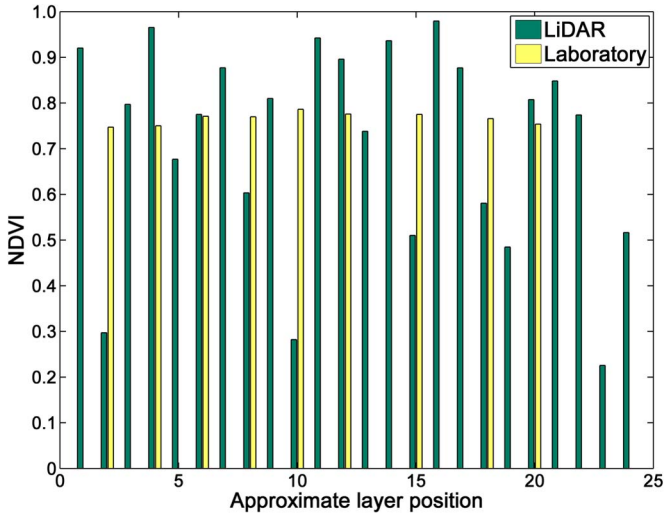

Fig. 13. Variation of NDVI as a function of depth from the top of the tree for LiDAR and laboratory data.

of the tree, and it has been observed that clumped canopies exhibit greater porosity and, hence, less reflectance [39].

Using the data from Table I and Fig. 8, we can compare the NDVIs of the needle samples as a function of depth into the canopy, as shown in Fig. 13.

The LiDAR data shown in green are numbered by layer, not equally spaced, and the yellow bars represent the approximately corresponding nine sample positions shown in Fig. 7. As one might expect from data such as that shown in Fig. 5, there is much greater standard deviation ($\mu = 0.713$, $\sigma = 0.226$) in the LiDAR than in the laboratory ($\mu = 0.766$, $\sigma = 0.0132$) data, but a standard t-test shows no significant difference between the computed mean NDVI values at the 1% level. Therefore, we can infer that the LiDAR measurement of NDVI corresponds to *in situ* measurements, but further experiment would be needed to see if we can extract small variations in photochemical profile data as shown in simulation [30].

VI. DETERMINING THE AREA AND ABUNDANCE PROFILES USING PARAMETER INVERSION

With known spectra, the area indices of needle and bark can be estimated from a set of overdetermined linear equations expressed in matrix notation, minimizing the norm $\|\rho A - \beta\|^2$ at each layer of the tree

$$\begin{pmatrix} \rho_{ni}^{531} & \rho_{bi}^{531} \\ \rho_{ni}^{570} & \rho_{bi}^{570} \\ \rho_{ni}^{670} & \rho_{bi}^{670} \\ \rho_{ni}^{780} & \rho_{bi}^{780} \end{pmatrix} \begin{pmatrix} A_n \\ A_b \end{pmatrix} = \begin{pmatrix} \beta_i^{531} \\ \beta_i^{570} \\ \beta_i^{670} \\ \beta_i^{780} \end{pmatrix}, \qquad i = 1 \ldots m \quad (4)$$

where ρ_{ni}^{λ} is the needle, ρ_{bi}^{λ} the bark reflectivity of the i th layer at wavelength λ, $A_{n/b}$ is the area of needles or bark proportional to the Spectralon area, having assumed 100% Lambertian reflectance, β_i^{λ} is the measured signal return amplitude at the corresponding wavelength and layer, and m is the number of layers recovered by the RJMCMC algorithm. These latter two terms are those in Table II, and the reflectance matrix is that

measured in the laboratory. (Of course, measuring these terms with respect to a known calibration target is not possible in airborne laser scanning, in which case it is necessary to compute the equivalent (to the Spectralon panel) response by use of the laser radar equation [39].) Hence, we apply Algorithm 2. This processes each layer iteratively, as part of the light is absorbed and reflected at each layer, part of the light is transmitted unaltered through the layer gap fraction, and, then, a small adjustment is made for needle transmittance. The measured spectra of Figs. 8 and 9 are used to compute these fractions.

Algorithm 2: Estimation of leaf and bark area index at successive layers. Gap refers to the layer gap area. Tr, Re, and Ab refer to material transmission, reflectance, and absorption so that light transmitted through the needles is added to the light at the next layer. It is assumed that no light is transmitted through bark.

$\lambda_j = \{\lambda_1, \ldots, \lambda_n\}, \quad \forall\, i = 1, \ldots m$
for each layer, $i = 1, \ldots, k$ {
    compute projected A_n and A_b using (4)
    compute actual needle and bark areas using
        estimates of projected area, relative reflectance
    for each λ (compute light transmitted to next layer)
{
$$Gap = 1 - (A_n + A_b)$$
$$Tr^{\lambda}_{ni} = 1 - (\mathrm{Re}^{\lambda}_{ni} + Ab^{\lambda}_{ni})$$
$$I_{i+1} = Gap * I^{\lambda}_i + Tr^{\lambda}_{ni} * I^{\lambda}_i$$
    }
}

However, there are several problems in forming an exact model of reflection in comparison with a calibration target or, indeed, using the laser radar equation. First, the base assumption is that needles and bark are randomly distributed in each layer, which is certainly not the case in practice as there are both clumping and correlated structure between layers. Smolander and Stenberg [41], [42] have studied the bidirectional reflectance distribution function (BRDF) of conifer samples and further studied light interception and clumping effects within conifer shoots to compute shoot silhouette area (SSA), which varies according to the angle of view. As an overall measure, they measured a spherically averaged ratio of intercepting SSA to total shoot area of 0.141, but at the normal direction, for the LiDAR, this is approximately doubled (see [42, Fig. 5]). To a first approximation, we use a ratio of 0.25, equivalent to a multiplier of the recovered projected area by 4 to get equivalent needle area.

The second problem is that measuring a response with respect to a calibration implies a normal Lambertian reflecting surface. In practice, the needle and bark distributions are not normal to the LiDAR axis. For example, North [43] suggests for Sitka spruce a leaf angle distribution, (0.15 0.20 0.18 0.15 0.13 0.09 0.05 0.03 0.02), in 10° increments from 0°–90° to the LiDAR axis. For Lambertian reflectance, the reflected light intensity would be proportional to the cosine of the LiDAR to surface normal angle, but Kaasalainen and Rautiainen [44] have shown that this is not a particularly good model for individual pine needles, as Greiner *et al.* [45] did for maple leaves. For the pine needles, there is no convenient analytic expression, but it was observed, for example, that there was a significant increase in measured needle brightness (1.13–1.79) at 0° compared to 3°–4° which is suggestive of significant specularity. We can approximate the observations of Kaasalainen and Rautiainen [44] by a Phong model with $\cos(\theta)$ and $\cos^{\alpha}(\theta)$ terms, and combining this with the interpolated needle distribution of North gives an approximate multiplier of 1.7 in the intensity of the needle model in comparison with the Spectralon target. In other words, the combination of a greater proportion of leaves aligned near the normal angle to the LiDAR beam with a Phong reflectance function based on single needle measurements overestimates the area.

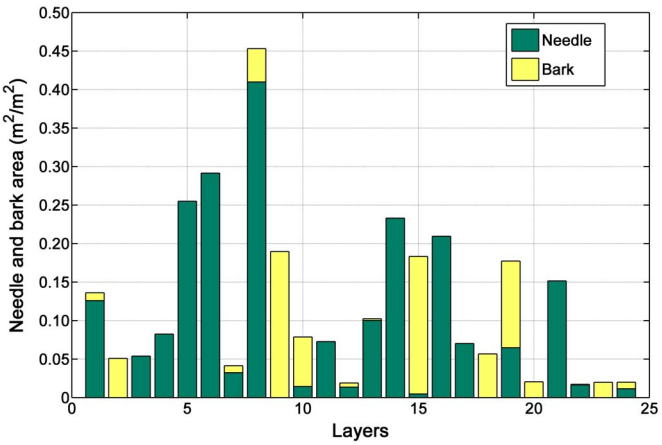

Fig. 14. Measured area profiles for leaf and bark as a function of canopy depth. These are measured as $\mathrm{m}^2/\mathrm{m}^2$ at the irregularly spaced layer positions shown in Fig. 6. This has no allowance for occlusion. The horizontal axis refers to the layer index.

A third problem is that the LiDAR has coaxial source and sensor geometry. A further correction factor can be applied to allow for occlusion, i.e., the probability of light interception of light with material at layer i is affected by the area of light interception at all the previous layers, $1 \ldots (i-1)$. We show results with and without this correction in Figs. 14 and 15, respectively.

Finally, there is the problem of multiple reflections. The coincident source-detector geometry with a focused spot size of approximately 5 mm means that backscatter from other sources or multiple reflections are very unlikely [25] in comparison with wide footprint LiDAR systems. Furthermore, in the simulation of Sitka spruce, Hancock [31] observed that the effect of multiple scattering was relatively small, increasing slightly the apparent reflectance but not affecting the overall shape of the waveform as the interreflection path lengths are very small within a single shoot.

The application of the algorithm to the real multispectral data gives the leaf and bark area profiles shown as the ratio of area of material to total area in each layer in Figs. 14 and 15. To the best of our knowledge, this is the first attempt to analyze such multispectral data in this manner, and the factors that we have discussed show that there is considerable uncertainty in the exact interpretation. We apply the SSA correction but

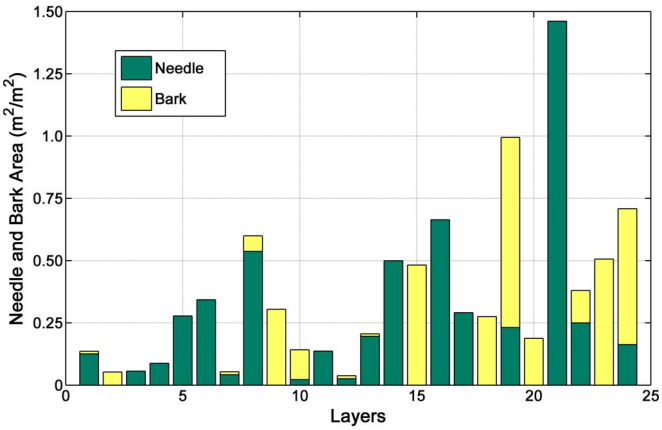

Fig. 15. Measured area profiles for leaf and bark as a function of canopy depth. These are measured as m^2/m^2 at the irregularly spaced layer positions shown in Fig. 6. This assumes a random distribution of areas in each layer so that subsequent layers have occluded material.

have not allowed for the possible hotspot effect caused by leaf inclination and specularity nor the lost light through multiple scattering outside the line of sight, as both are more speculative and cancel each other approximately. We show data that ignore and allow for occlusion.

The results presented here, while variable and not directly validated in this study, do indicate that taking occlusion into consideration presents a distribution of foliage and bark consistent with previously published material [46], which lends support to the processing sequences presented here. However, a rigorous validation of this retrieval is desirable.

VII. Conclusion

We have constructed a novel multispectral LiDAR instrument based on a supercontinuum laser source and time-correlated photon counting receiver technology designed specifically to recover structural and physiological parameters from tree samples. Using that instrument, we have scanned a small Nordmann fir sample and extracted full waveform data at four wavelengths corresponding to the NDVI and PRI indices. We have compared the NDVI depth profile measured by the system with validatory laboratory measurements using a spectrometer to show good agreement.

We have further developed our RJMCMC methodology for the analysis of LiDAR waveforms to interpret the multispectral data. Using a single wavelength, the analysis is able to resolve single surface depth returns to centimeter resolution, well in excess of current deployed LiDAR instrumentation and associated algorithms for their interpretation. Using multiple wavelengths, we have recovered abundance profiles and area indices as a function of depth into the sample. Our layered model to represent the crown or canopy is also innovative, as it can adapt to different tree structures by varying the layer positions to fit the dominant foliage patterns, as shown by the remarkably good fit of the layered model to the real data. As yet, we do use a number of constraints and assumptions about the distribution of needle orientation, the needle BRDF, and the progressive transmittance of light between layers. However, our results confirm our own previous work on monochromatic LiDAR signals and multispectral simulations to demonstrate that MCSL is a serious option to combine structural and physiological data gathering from arboreal samples. As far as possible, we have also compared our results with other studies in the literature, and these also show consistency of interpretation.

There are several areas for further investigation. We have observed variations in the spectral response at different pixel sites. Bearing in mind that we are (almost) point sampling with a 3-mm-diameter beam, this could well just be due to different material impacts, but it does raise questions about the validity of detailed simulations by ourselves and other authors as we are measuring real samples at resolutions comparable to the graphical models which use polygonal data (e.g., Onyxtree at www.onyxtree.com).

We have also explained that the full parameter recovery problem is ill posed with only four wavelengths, as variation in spectra can be confused with different material mixture proportions. We propose that a deployed instrument would benefit greatly from an extended set of eight wavelengths, as discussed in Section IV. Furthermore, we aim to measure from full canopy, as opposed to single tree data, as a first step toward eventual possible air and space deployment which we have considered in separate studies. In such a deployed instrument, it is necessary to ascertain the most efficient sampling methodology. Currently, high power lasers produced integrated returns from wide footprints at sparsely sampled [in (x, y)] locations. If a high repetition rate using photon counting is deployed, one would acquire much more closely spaced random samples from a continuously scanned area.

References

[1] C. J. Nichol, K. F. Huemmrich, T. A. Black, P. G. Jarvis, C. L. Whitehall, J. Grace, and F. G. Hall, "Remote sensing of photosynthetic-light-use efficiency of boreal forest," *Agricultural and Forest Meteorology*, vol. 101, no. 2/3, pp. 131–142, Mar. 2000.

[2] I. H. Woodhouse, C. Nichol, G. Patenaude, and T. J. Malthus, "Patent Application for a MSCL Remote Sensing System," Publication No. U.S. 2011/0101239 A1, May 5, 2011.

[3] I. H. Woodhouse, J. Jack, E. Rumi, D. Henry, M. MacDonald, N. Bezawada, C. Nichol, G. Patenaude, and R. Pfab, "Early mission concept for a spaceborne multi-spectral LiDAR," NCEO Feasibility Study Report, Commercial in Confidence, p. 149, Jan. 2012.

[4] G. le Maire, C. Francois, K. Soudani, D. Bervellier, J.-Y. Pontailler, N. Breda, H. Genet, H. Davi, and E. Dufrene, "Calibration and validation of hyper-spectral indices for the estimation of broadleaved forest leaf chlorophyll content, leaf mass per area, leaf area index and leaf canopy biomass," *Remote Sens. Environ.*, vol. 112, no. 10, pp. 3846–3864, Oct. 2011.

[5] J. Hill, "State-of-the-Art and Review of Algorithms with Relevance for Retrieving Biophysical and Structural Information on Forests and Natural Vegetation with Hyper-Spectral Remote Sensing Systems," Potsdam, Germany, Sci. Tech. Rep. STR10/08, 2010, *Hyper-spectral Algorithms*, Chapter 3 in H. Kaufmann, K. Segl, S. Itzerott, H. Bach, A. Wagner, J. Hill, B. Heim, K. Oppermann, W. Heldens, E. Stein, A. Müller, S. van der Linden, P. J. Leitão, A. Rabe, P. Hostert.

[6] L. Suarez, P. J. Zarco-Tejada, J. A. J. Berni, V. Gonzalez-Dugo, and E. Fereres, "Modelling PRI for water stress detection using radiative transfer models," *Remote Sens. Environ.*, vol. 113, no. 4, pp. 730–744, Apr. 2009.

[7] P. J. Zarco-Tejada, A. Berjon, R. Lopez-Lozano, J. R. Miller, P. Martin, V. Cachorro, M. R. Gonzalez, and A. de Frutos, "Assessing vineyard condition with hyper-spectral indices: Leaf and canopy reflectance simulation in a row-structured discontinuous canopy," *Remote Sens. Environ.*, vol. 99, no. 3, pp. 271–287, Nov. 2005.

[8] N. Keshava, "A survey of spectral unmixing algorithms," *Lincoln Lab. J.*, vol. 14, no. 1, pp. 55–78, 2003.
[9] M. Parente and A. Plaza, "Survey of geometric and statistical unmixing algorithms for hyper-spectral images," in *Proc. 2nd Workshop Hyper-Spectral Image Signal Process., Evol. Remote Sens.*, 2010, pp. 1–4.
[10] C. W. Xiao and R. Ceulemans, "Allometric relationships for below- and above-ground biomass of young Scots pines," *Forest Ecol. Management*, vol. 203, no. 1-3, pp. 177–186, Dec. 2004.
[11] M. Xu and T. B. Harrington, "Foliage biomass distribution of loblolly pine as affected by tree dominance, crown size, and stand characteristics," *Can. J. Forest Res.*, vol. 28, no. 6, pp. 887–992, 1998.
[12] D. A. Maguire and W. S. Bennet, "Patterns in vertical distribution of foliage in young coastal Douglas fir," *Can. J. Forest Res.*, vol. 26, no. 11, pp. 1991–2005, Nov. 1996.
[13] P. J. Leitão, A. Rabe, P. Hostert, A. Rosenqvist, A. Milne, R. Lucas, M. Imhoff, and C. Dobsone, "A review of remote sensing technology in support of the Kyoto protocol," *Environ. Sci. Policy*, vol. 6, pp. 441–455, 2003.
[14] M. Garcia, D. Riano, E. Chuvieco, and R. M. Danson, "Estimating biomass carbon stocks for a Mediterranean forest in central Spain using LiDAR height and intensity data," *Remote Sens. Environ.*, vol. 114, no. 4, pp. 816–830, Apr. 2010.
[15] F. G. Hall, K. Bergen, J. B. Blair, R. Dubayah, R. Houghton, G. Hurtt, J. Kellndorfer, M. Lefsky, J. Ranson, S. Saatchi, H. H. Shugart, and D. Wickland, "Characterizing 3D vegetation structure from space: Mission requirements," *Remote Sens. Environ.*, vol. 115, no. 11, pp. 2753–2775, Nov. 2011.
[16] C. Mallet and F. Bretar, "Full waveform topographic lidar: State of the art," *ISPRS J. Photogramm. Remote Sens.*, vol. 64, no. 1, pp. 1–16, Jan. 2009.
[17] M. van Leuwen and M. Nieuwenhuis, "Retrieval of forest structural parameters using LiDAR remote sensing," *Eur. J. Forest Res.*, vol. 129, no. 4, pp. 749–770, Jul. 2010.
[18] D. J. Selkowitz, G. Green, B. Peterson, and B. Wylie, "A multi-sensor LiDAR, multi spectral and multi angular approach for mapping canopy height in boreal forest regions," *Remote Sens. Environ.*, vol. 121, pp. 458–471, Jun. 2012.
[19] J. E. Anderson, L. C. Plourde, M. E. Martin, B. H. Braswell, M.-L. Smith, R. O. Dubayah, M. A. Hofton, and J. Bryan Blair, "Integrating waveform LiDAR with hyper-spectral imagery for inventory of a northern temperate forest," *Remote Sens. Environ.*, vol. 112, no. 4, pp. 1856–1870, Apr. 2008.
[20] A. Swatantran, R. Dubayah, D. Roberts, M. Holton, and J. Bryan Blair, "Mapping biomass and stress in the Sierra Nevada using LiDAR and hyper-spectral data fusion," *Remote Sens. Environ.*, vol. 115, no. 11, pp. 2917–2930, Nov. 2011.
[21] P. Dabney, D. J. Harding, J. Abshire, T. Huss, G. Jodor, R. Machan, J. Marzouk, K. Rush, A. Seas, C. Shuman, X. Sun, S. Valett, A. Vasilyev, A. Yu, and Y. Zheng, "The slope imaging multi-polarization photon-counting LiDAR," in *Proc. SPIE Geosci. Remote Sens. Symp.*, 2010, pp. 653–656.
[22] J. Suomalainen, T. Hakala, H. Kaartinen, E. Raikkonen, and S. Kaasalainen, "Demonstration of a virtual active hyper-spectral LiDAR in automated point cloud classification," *ISPRS J. Photogramm. Remote Sens.*, vol. 66, no. 5, pp. 637–641, Sep. 2011.
[23] T. Hakala, J. Suomalainen, S. Kaasalainen, and Y. Chen, "Full waveform hyper-spectral LiDAR for terrestrial laser scanning," *Opt. Exp.*, vol. 20, no. 7, pp. 7119–7127, Mar. 2012.
[24] G. Wei, S. Shalei, Z. Bo, S. Shuo, L. Faquan, and C. Xuewu, "Multi-wavelength canopy LiDAR for remote sensing of vegetation: Design and system performance," *ISPRS J. Photogramm. Remote Sens.*, vol. 69, pp. 1–9, Apr. 2012.
[25] G. S. Buller, R. D Harkins, A. McCarthy, P. A. Hiskett, G. MacKinnon, G. Smith, R. Sung, A. M. Wallace, and R. Lamb, "A multiple wavelength time-of-flight sensor based on time-correlated single-photon counting," *Rev. Sci. Instrum.*, vol. 76, no. 8, p. 083112, 2005.
[26] C. Tucker, "Red and photographic infrared linear combinations for monitoring vegetation," *Remote Sens. Environ.*, vol. 8, no. 2, pp. 127–150, May 1979.
[27] M. F. Garbulsky, J. Peñuelas, J. Gamonc, Y. Inoue, and I. Filella, "The photochemical reflectance index (PRI) and the remote sensing of leaf, canopy and ecosystem radiation use efficiencies: A review and meta-analysis," *Remote Sens. Environ.*, vol. 115, no. 2, pp. 281–297, Feb. 2011.
[28] I. H. Woodhouse, C. Nichol, P. Sinclair, J. Jack, F. Morsdorf, T. Malthus, and G. Patenaude, "A multi-spectral canopy LiDAR demonstrator project," *IEEE Geosci. Remote Sens. Lett.*, vol. 8, no. 5, pp. 839–843, Sep. 2011.
[29] S. Hernandez-Marin, A. M. Wallace, and G. J. Gibson, "Bayesian analysis of LiDAR signals with multiple returns," *IEEE Trans. Pattern Anal. Mach. Intell.*, vol. 29, no. 12, pp. 2170–2180, Dec. 2007.
[30] A. M. Wallace, C. J. Nichol, and I. H. Woodhouse, "Recovery of forest canopy parameters by inversion of multi-spectral data," *Remote Sens.*, vol. 4, no. 2, pp. 509–531, 2012.
[31] S. Hancock, "Understanding the measurement of forests with waveform LiDAR," Ph.D. dissertation, Univ. College London, London, U.K., 2010.
[32] F. Morsdorf, C. Nichol, T. Malthus, and I. H. Woodhouse, "Assessing forest structural and physiological information content of multi-spectral LiDAR waveforms by radiative transfer modeling," *Remote Sens. Environ.*, vol. 113, no. 10, pp. 2152–2163, Oct. 2009.
[33] A. McCarthy, R. J. Collins, N. J. Krichel, V. Fernández, A. M. Wallace, and G. S. Buller, "Long-range time-of-flight scanning sensor based on high-speed time-correlated single-photon counting," *Appl. Opt.*, vol. 48, no. 32, pp. 6241–6251, Nov. 2009.
[34] A. McCarthy, N. J. Krichel, N. R. Gemmell, X. Ren, M. G. Tanner, S. N. Dorenbos, V. Zwiller, R. H. Hadfield, and G. S. Buller, "Kilometer-range, high resolution depth imaging via 1560 nm wavelength single-photon detection," *Opt. Exp.*, vol. 21, no. 7, pp. 8904–8915, Apr. 2013.
[35] S. Jaquemoud, W. Verhoef, F. Baret, C. Bacour, P. J. Zarco-Tejada, G. P. Asner, C. Francois, and S. L. Ustin, "Prospect+Sail models: A review of use for vegetation characterization," *Remote Sens. Environ.*, vol. 113, no. 1, pp. S56–S66, Sep. 2009.
[36] Z. Malenovsky, J. Albrectova, Z. Lhotakova, R. Zurita-Milla, J. G. P. W. Clevers, M. E. Schaepmann, and P. Cudlin, "Applicability of the Prospect model for Norway spruce needles," *Int. J. Remote Sens.*, vol. 27, no. 24, pp. 5315–5340, 2006.
[37] J. Verrelst, M. E. Schaepmann, Z. Malenovsky, and J. G. P. W. Clevers, "Effects of woody elements on simulated canopy reflectance: Implications for forest chlorophyll content retrieval," *Remote Sens. Environ.*, vol. 114, no. 3, pp. 647–656, Mar. 2010.
[38] F. J. Garcia-Haro, M. A. Gilabert, and J. Melia, "A radiosity model for heterogeneous canopies in remote sensing," *J. Geophys. Res.*, vol. 104, no. D10, pp. 12 159–12 175, May 1999.
[39] D. da Silva, F. Boudon, C. Godin, and H. Sinoquet, "Multiscale framework for modeling and analysing light interception by trees," *Multiscale Model. Simul.*, vol. 7, no. 2, pp. 910–933, 2008.
[40] W. Wagner, A. Ullrich, V. Ducic, T. Melzer, and N. Studnick, "Gaussian decomposition and calibration of a novel small-footprint full-waveform digitising airborne laser scanner," *ISPRS J. Photogramm. Remote Sens.*, vol. 60, no. 2, pp. 100–112, Apr. 2006.
[41] S. Smolander and P. Stenberg, "A method for estimating light interception by a conifer shoot," *Tree Physiol.*, vol. 21, no. 12/13, pp. 797–803, Aug. 2001.
[42] S. Smolander and P. Stenberg, "A method to account for shoot scale clumping in coniferous canopy reflectance models," *Remote Sens. Environ.*, vol. 88, pp. 363–373, 2003.
[43] P. R. J. North, "Three-dimensional forest light interaction using a Monte Carlo method," *IEEE Trans. Geosci. Remote Sens.*, vol. 34, no. 4, pp. 946–956, Jul. 1996.
[44] S. Kaasalainen and M. Rautiainen, "Backscattering measurements from individual Scots pine needles," *Appl. Opt.*, vol. 46, no. 22, pp. 4916–4922, Aug. 2007.
[45] M. A. Greiner, B. D. Duncan, and M. P. Dierking, "Monte Carlo simulation of multiple photon scattering in sugar maple tree canopies," *Appl. Opt.*, vol. 48, no. 32, pp. 6159–6171, Nov. 2009.
[46] H. Temesgen and A. R. Weiskittel, "Leaf mass per area relationships across light gradients in hybrid spruce crowns," *Trees-Structure Function*, vol. 20, no. 4, pp. 522–530, Jun. 2006.

Andrew M. Wallace received the B.Sc. and Ph.D. degrees from The University of Edinburgh, Edinburgh, U.K., in 1972 and 1975, respectively.

He is a Professor of Signal and Image Processing with Heriot-Watt University, Edinburgh, U.K. His research interests include vision, image, and signal processing and parallel many-core architectures. He has published extensively, receiving a number of best paper and other awards, and has secured funding from EPSRC, the European Union (EU), and other industrial and government sponsors.

Prof. Wallace is a Chartered Engineer and a Fellow of the Institute of Engineering Technology.

Aongus McCarthy received the B.Sc. degree from University College, Galway, Ireland, in 1989, the Diploma degree in electronic engineering from the Institute of Technology, Carlow, Ireland, in 1990, and the B.Sc. degree in physical optoelectronics from Essex University, Essex, U.K., in 1991. He then worked in industry before completing the Ph.D. degree in physics from Heriot-Watt University, Edinburgh, U.K., in 2002.

He is currently with the School of Engineering and Physical Sciences, Heriot-Watt University. His research interests include optical and optomechanical system design, time-of-flight laser ranging, single-photon counting technologies, and microscope systems.

Dr. McCarthy is a member of the Optical Society of America and the IEEE Photonics Society.

Caroline J. Nichol received the B.Sc. and Ph.D. degrees from The University of Edinburgh, Edinburgh, U.K., in 1997 and 2000, respectively.

She is currently a Senior Lecturer in remote sensing with the School of Geosciences, The University of Edinburgh, with research interests focusing on the use of passive (airborne and satellite) data as well as light detection and ranging data to infer forest structure and physiology.

Dr. Nichol recently (2011) became a member of the Royal Society of Edinburgh Young Academy of Scotland.

Ximing Ren received the B.Sc. degree in optical information engineering from the Beijing Institute of Technology, Beijing, China, in 2008. He worked in photoelectronic imaging at Beihang University, Beijing, and received the M.Sc. degree of electronics science and technology in 2011.

In 2011, he started a Ph.D. with the Photon Counting group, studying time-of-flight photon counting laser ranging under the supervision of Prof. Gerald Buller.

Simone Morak received the M.Sc. degree from the University of Innsbruck, Innsbruck, Austria, in 2008 and the Ph.D. degree from The University of Edinburgh, Edinburgh, U.K., in 2012.

She worked as a Research Assistant for Dr. Caroline Nichol at The University of Edinburgh, from 2011 to 2012. She then joined Fugro GEOS Ltd., where she was employed as an Atmospheric Modeller. She has now joined the University of Reading as a Research Associate.

Daniel Martinez-Ramirez received the B.Sc. degree from the Instituto Tecnologico de Cd. Madero, Madero, Mexico, in 1999 and M.Sc. degrees from the InstitutoTecnologico y de Estudios Superiores de Monterrey, Monterrey, Mexico, in 2001. He is currently working toward the Ph.D. degree on multispectral light detection and ranging processing at Heriot-Watt University, Edinburgh, U.K.

Mr. Martinez-Ramirez is a student member of the IEEE Signal Processing and the IEEE Geoscience and Remote Image Society.

Iain H. Woodhouse received the B.Sc. degree from The University of Edinburgh, Edinburgh, U.K., the M.Sc. degree in remote sensing from the University of Dundee, Dundee, U.K., and the Ph.D. degree from Heriot-Watt University, Edinburgh.

Since 1999, he has been with The University of Edinburgh, currently a Senior Lecturer in radar remote sensing with the School of Geosciences. He is a member of the U.K. National Space Technology Steering Group, a Director of Carbomap, Ltd., and a cofounder of Ecometrica Ltd. He was the Founding Head of the Edinburgh Earth Observatory.

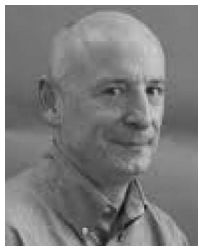

Gerald S. Buller received the B.Sc. degree in natural philosophy from the University of Glasgow, Glasgow, U.K., in 1986 and the Ph.D. degree in physics from Heriot-Watt University, Edinburgh, U.K., in 1989.

In 2002, he founded Helia Photonics, Ltd. He is currently a Professor of physics with Heriot-Watt University. He is an author of more than 100 papers published in major international journals. His research interests include aspects of single-photon detection, including infrared single-photon detectors, depth imaging, quantum cryptography, and quantum imaging.

Prof. Buller is a Fellow of the Institute of Physics, a member of the Optical Society of America, and a Fellow of the Royal Society of Edinburgh.